TABLE VI
Small- and Medium-Scale Test Hub Positions

Data Set	Polarization	Total Displacement (cm) from Start
1/2	Vertical/Horizontal	0.0
3/4	Vertical/Horizontal	1.7
5/6	Vertical/Horizontal	2.5
7/8	Vertical/Horizontal	3.8
9/10	Vertical/Horizontal	5.0
11/12	Vertical/Horizontal	10.1
13/14	Vertical/Horizontal	15.2
15/16	Vertical/Horizontal	20.3
17/18	Vertical/Horizontal	25.4
21/22	Vertical/Horizontal	20.5
23/24	Vertical/Horizontal	50.8
25/26	Vertical/Horizontal	91.4
27/28	Vertical/Horizontal	111.7
29/30	Vertical/Horizontal	132.1
31/32	Vertical/Horizontal	172.7
33/34	Vertical/Horizontal	213.4
35/36	Vertical/Horizontal	254.0
37/38	Vertical/Horizontal	294.6
39/40	Vertical/Horizontal	335.8

RICHARD KETCHAM
JEFF FROLIK
Dept. of Electrical and Computer Engineering
University of Vermont
33 Colchester Ave.
Burlington, VT 05405
E-mail: (jfrolik@uvm.edu)

JOHN COVELL
Goodrich Corporation
Fuel and Utility Systems
Vergennes, VT

REFERENCES

[1] Pottie, G., and Kaiser, W.
Wireless integrated network sensors.
Communications of the ACM, **43**, 5 (May 2000), 51–58.

[2] Estrin, D., Girod, L., Pottie, G., and Srivastava, M.
Instrumenting the world with wireless sensor networks.
In *Proceedings of the International Conference on Acoustics, Speech and Signal Processing* (ICASSP 2001).

[3] MIT Technology Review
10 emerging technologies that will change the world.
MIT Technology Review, Feb. 2003.

[4] Furse, C., Chung, Y., Lo, C., and Pendayala, P.
A critical comparison of reflectometry methods for location of wiring raults.
Smart Structures and Systems, **2**, 1 (2006), 25–46.

[5] Wireless Smoke Detection
Online: http://www.securaplane.com/smoke2.html, Securaplane Technologies Inc. (21Nov06).

[6] St. John, E.
Operational issues wireless overview.
Presented at the World Airline Entertainment Association Single Focus Workshop (WAEA SFW), Washington, D.C., Nov. 19–20, 2002.

[7] Securaplane Technologies, Inc.
Press Release, "Securaplane Technologies Awarded Boeing 787 Contract for Wireless Emergency Lighting," Dec. 21, 2004.
Online: http://www.securaplane.com/releases/pr0095.html (21Nov06).

[8] Fitzhugh, C., and Frolik, J., Ketcham, R., Covell, J., and Meyer, T.
2.4 GHz multipath environments in airframes.
Presented at the IEEE Conference on Wireless and Microwave Technology (WAMICON 2005), Clearwater, FL, Apr. 7–8, 2005.

[9] Frolik, J.
A case for considering hyper-Rayleigh fading.
IEEE Transactions on Wireless Communications, **6**, 4 (Apr. 2007).

[10] Durgin, G., Rappaport, T., and de Wolf, D.
New analytical models and probability density functions for fading in wireless communications.
IEEE Transactions on Communications, **50**, 6 (June 2002).

[11] Chong, C-C., and Yong, S.
A generic statistical-based UWB channel model for high-rise apartments.
IEEE Transactions on Antennas and Propagation, **53**, 8 (Aug. 2005), 2389–99.

[12] Rappaport, T.
Rayleigh and Ricean distributions.
In *Wireless Communication Systems: Principles and Practice*, (2nd ed.), Upper Saddle River, NJ: Prentice-Hall, 2002, sect. 5.6.

Adaptive Detection and Diversity Order in Multistatic Radar

We derive the generalized likelihood ratio test (GLRT) for multistatic space-time radar where each sensor platform has a coherent multi-channel array. A multistatic version of the adaptive matched filter (AMF) detector is also developed and its performance results compared with that of the GLRT. Results show that the multistatic GLRT outperforms the multistatic AMF and that the performance advantage increases with the number of radars in the system. The concepts of geometry gain and diversity gain for multistatic STAP are defined in terms of asymptotic properties of the system's probability of miss.

I. INTRODUCTION

Space-time adaptive processing (STAP) is an extension of adaptive antenna techniques that uses the signals received on multiple elements of an array and multiple pulses of a coherent processing interval (CPI) to form a space-time filter that maximizes system signal-to-noise ratio (SNR). The benefits of this filtering technique are enhanced detection performance

Manuscript received February 6, 2007; revised December 7, 2007; released for publication April 21, 2008.

IEEE Log No. T-AES/44/4/930746.

Refereeing of this contribution was handled by M. Rangaswamy.

and improved rejection of external interference [1–3].

Even though STAP is a powerful technique in clutter cancellation, certain radar/target geometries are less favorable than others, and ground-based interference is still a significant factor in most circumstances. If the target velocity vector is approximately perpendicular to the radar platform's line of sight, the target will be hard to distinguish from background clutter. However, this can be overcome by adding additional viewing perspectives that realize more radial velocity from the target. Furthermore, we show below that the number of radar platforms observing a fluctuating target controls the asymptotic slope of the system's probability-of-miss (P_{m}) performance while the specific geometry controls the asymptotic shift.

The system that we study here is a multistatic radar system made up of widely separated airborne platforms. Each platform is capable of acting as both transmitter and receiver. As a receiver, each platform possesses a coherent, multi-channel array capable of collecting a space-time data set. Furthermore, we also assume that each receiver can collect and separate the data due to multiple transmitters, which requires separable waveforms. For example, multiple waveforms can be separated when transmitted on nonoverlapping frequency bands. The multistatic system consists of several unique propagation paths. First, there are monostatic paths where receivers measure reflections due to their co-platform transmitters. Second, there are bistatic paths where receivers measure reflections due to the waveforms transmitted from different platforms.

Multistatic radar has the advantage of viewing the same target from multiple perspectives. As described in [4], in the presence of ground clutter this provides two types of performance gains: diversity gain and geometry gain. Diversity gain is obtained by observing multiple independent observations of a fluctuating target. For example, the MIMO radar work of [5]–[6] shows how these fluctuations can be exploited. The work in [5]–[6] considers spectrally white interference. For multistatic STAP, however, the effectiveness of these multiple observations is controlled by how well ground clutter and other interference can be rejected. This rejection, in turn, depends on the geometry of the radar platform and the target's velocity vector. Fortunately, a moving target that has no radial velocity with respect to one radar will likely have some radial velocity with respect to a second radar provided there is enough spatial displacement between the two viewing perspectives. Hence, geometry controls the diversity gain, and we have called this factor the geometry gain.

In this paper, we derive constant false-alarm rate (CFAR) detectors for multistatic STAP and quantify their performance in terms of diversity and geometry gain. The CFAR detectors are multistatic extensions of the monostatic CFAR tests of [7] and [8]. We compute P_{m} and show that in the presence of a fluctuating target, P_{m} curves for both CFAR tests possess an asymptotic slope. This asymptotic behavior is analogous to the probability-of-outage behavior used to define diversity order (DO) in communication theory. Therefore, we propose definitions of diversity and geometry gain in terms of the asymptotic behavior.

In the next section, we define our problem statement and signal model. Section II also develops the multistatic versions of the GLRT and AMF detection methods and discusses their statistical properties. Section III presents the results from a series of experiments using the detection methods developed in Section II. These experiments not only compare the methods as a function of number of radars employed, but also outline a way to characterize which geometries optimize performance for a given multistatic configuration. Also discussed in Section III is the performance increase associated with including bistatic paths between radars as a means of increasing diversity gain without increasing the number of radar platforms. Section IV concludes the paper.

II. SIGNAL MODEL AND DETECTION STATISTICS

A. Multistatic STAP Signal Model

Let a multistatic radar system be comprised of multiple airborne platforms at different locations surrounding an area of interest. Each platform possesses a multi-channel array; therefore, the system model is defined by Q independent sets of space-time observations of the same area on the ground. In the context of this paper, independent observations can be realized by geographical separation of the radar platforms and from both monostatic and bistatic propagation paths.

Let the primary data corresponding to the qth space-time data set be denoted by the vector $\mathbf{z}_q$ for $1 \le q \le Q$. Each $\mathbf{z}_q$ is formed by stacking the space-time data samples collected by a local multi-antenna array over multiple pulses into a column vector where the length N_q is the number of space-time measurements observed in a single snapshot of the qth data set. The qth primary data vector is defined as

$$\begin{aligned} H_0: &\quad \mathbf{z}_q = \mathbf{n}_q \\ H_1: &\quad \mathbf{z}_q = b_q \mathbf{s}_q + \mathbf{n}_q. \end{aligned} \tag{1}$$

In (1), $\mathbf{n}_q$ is the vector of noise and interference corrupting the qth data set, $\mathbf{s}_q$ is the normalized space-time steering vector for the target hypothesis relative to the specific propagation geometry of the qth data set, and b_q is the complex amplitude of the

target signature in the qth data set. H_0 is the null hypothesis, and H_1 is the target-present hypothesis. The interference vector $\mathbf{n}_q$ is a zero-mean complex Gaussian process characterized by the covariance matrix $\mathbf{M}_q$. The noise vectors are assumed to be independent from data set to data set.

Since the target's absolute position and velocity vector map into different relative angles and Doppler shifts for different data sets, each steering vector $\mathbf{s}_q$ is different even though they describe the same absolute target hypothesis. Therefore, the mapping of hypotheses from absolute parameters to relative parameters must be very accurate, which implies accurate knowledge of the relative locations of the radar platforms. If the mapping is inaccurate, the target may still be detected, but estimates of the target's absolute position and velocity may be inaccurate due to improper alignment of the relative hypotheses of each platform. In this paper, we do not address how the mapping of relative hypotheses takes place, nor do we quantify the effects of inaccurate mapping on detection or parameter estimation.

B. Multistatic STAP Generalized Likelihood Ratio Test

Let $\mathbf{Z}_q$ be a matrix of space-time measurements that comprise the qth data set. This matrix is defined as $\mathbf{Z}_q = [\mathbf{z}_q \ \mathbf{z}_q(1) \ \mathbf{z}_q(2) \cdots \mathbf{z}_q(K_q)]$ where $\mathbf{z}_q$ is the primary data vector defined above, and $\mathbf{z}_q(1),\ldots,\mathbf{z}_q(K_q)$ are K_q secondary data vectors. The $\mathbf{Z}_q$s combine to form the full matrix of observations due to all Q data sets, $\mathbf{Z} = [\mathbf{Z}_1 \ \mathbf{Z}_2 \cdots \mathbf{Z}_Q]$. Due to the independence of the interference between data sets, the joint probability density function (pdf) of all data matrices from all radar platforms reduces to a product of the individual pdfs from each of the data sets. The joint pdfs for the H_0 and H_1 hypotheses for Q data sets are

$$f(\mathbf{Z} \mid H_0) = f(\mathbf{Z}_1,\mathbf{Z}_2,\ldots,\mathbf{Z}_Q \mid H_0) = \prod_{q=1}^{Q} f_q(\mathbf{Z}_q \mid H_0)$$
$$f(\mathbf{Z} \mid H_1) = f(\mathbf{Z}_1,\mathbf{Z}_2,\ldots,\mathbf{Z}_Q \mid H_1) = \prod_{q=1}^{Q} f_q(\mathbf{Z}_q \mid H_1). \tag{2}$$

Under the H_0 hypothesis, the primary data vector has the same pdf as the secondary data. Since clutter returns are assumed to be complex Gaussian, the null hypothesis pdf for a single data vector and data set can be represented as

$$f_q(\mathbf{z}_q(k) \mid H_0) = \frac{1}{\pi^{N_q}\|\mathbf{M}_q\|} \exp[-\mathbf{z}_q^{\mathrm{H}}(k)\mathbf{M}_q^{-1}\mathbf{z}_q(k)] \tag{3}$$

where $(\cdot)^{\mathrm{H}}$ denotes the conjugate transpose operation and $\|\cdot\|$ denotes the determinant of a matrix. In (3), $\mathbf{M}_q$ is the interference covariance that applies to the qth data set; therefore, $\mathbf{M}_q = \mathrm{E}\{\mathbf{z}_q(k)\mathbf{z}_q^{\mathrm{H}}(k)\}$ where $\mathrm{E}\{\cdot\}$ denotes expected value. Equation (3) also applies to all $\mathbf{z}_q(k)$ under the H_1 hypothesis, but the pdf for the primary data vector under H_1 is

$$f_q(\mathbf{z}_q \mid H_1) = \frac{1}{\pi^{N_q}\|\mathbf{M}_q\|} \exp[-(\mathbf{z}_q - b_q\mathbf{s}_q)^{\mathrm{H}}\mathbf{M}_q^{-1}(\mathbf{z}_q - b_q\mathbf{s}_q)]. \tag{4}$$

If the space-time data snapshots within a given data set are independent, the pdf for that data set is

$$\begin{aligned} f_q(\mathbf{Z}_q \mid H_0) &= f_q(\mathbf{z}_q,\mathbf{z}_q(1),\ldots,\mathbf{z}_q(K_q) \mid H_0) \\ &= f_q(\mathbf{z}_q \mid H_0)\prod_{k=1}^{K_q} f_q(\mathbf{z}_q(k) \mid H_0) \\ f_q(\mathbf{Z}_q \mid H_1) &= f_q(\mathbf{z}_q,\mathbf{z}_q(1),\ldots,\mathbf{z}_q(K_q) \mid H_1) \\ &= f_q(\mathbf{z}_q \mid H_1)\prod_{k=1}^{K_q} f_q(\mathbf{z}_q(k) \mid H_0). \end{aligned} \tag{5}$$

Using the identity $\mathbf{v}^{\mathrm{H}}\mathbf{A}^{-1}\mathbf{v} = \mathrm{tr}[\mathbf{A}^{-1}\mathbf{V}]$ where $\mathbf{v}$ is a vector, $\mathbf{A}$ is a square matrix, $\mathbf{V} = \mathbf{v}\mathbf{v}^{\mathrm{H}}$, and $\mathrm{tr}[\cdot]$ is the matrix trace operator, we can derive

$$f_q(\mathbf{Z}_q \mid H_0) = \left\{\frac{1}{\pi^{N_q}\|\mathbf{M}_q\|}\exp[-\mathrm{tr}(\mathbf{M}_q^{-1}\mathbf{T}_{q|H_0})]\right\}^{K_q+1} \tag{6}$$

and

$$f_q(\mathbf{Z}_q \mid H_1) = \left\{\frac{1}{\pi^{N_q}\|\mathbf{M}_q\|}\exp[-\mathrm{tr}(\mathbf{M}_q^{-1}\mathbf{T}_{q|H_1})]\right\}^{K_q+1} \tag{7}$$

where

$$\begin{aligned} \mathbf{T}_{q|H_0} &= \frac{1}{K_q+1}\left(\mathbf{z}_q\mathbf{z}_q^{\mathrm{H}} + \sum_{k=1}^{K_q}\mathbf{z}_q(k)\mathbf{z}_q^{\mathrm{H}}(k)\right) \\ \mathbf{T}_{q|H_1} &= \frac{1}{K_q+1}\left((\mathbf{z}_q - b_q\mathbf{s}_q)(\mathbf{z}_q - b_q\mathbf{s}_q)^{\mathrm{H}} + \sum_{k=1}^{K_q}\mathbf{z}_q(k)\mathbf{z}_q^{\mathrm{H}}(k)\right). \end{aligned} \tag{8}$$

The likelihood ratio test (LRT) is

$$\Lambda(\mathbf{Z}) = \frac{f(\mathbf{Z} \mid H_1)}{f(\mathbf{Z} \mid H_0)} = \prod_{q=1}^{Q}\frac{f_q(\mathbf{Z}_q \mid H_1)}{f_q(\mathbf{Z}_q \mid H_0)}. \tag{9}$$

To obtain the GLRT, the numerator and denominator of (9) are independently maximized over their respective unknown variables, which in this case includes all b_qs and $\mathbf{M}_q$s. Fortunately, both the numerator and denominator of (9) can be maximized by maximizing each of the $f_q(\mathbf{Z}_q \mid H_i)$ terms individually. Moreover, maximizing an individual term is the same problem solved in [7] to derive the monostatic STAP GLRT. Under the H_0 hypothesis, maximization of the qth term is accomplished by

the covariance estimate $\hat{\mathbf{M}}_{q|H_0} = \mathbf{T}_{q|H_0}$. Under the H_1 hypothesis, the maximization is accomplished by the covariance estimate $\hat{\mathbf{M}}_{q|H_1} = \mathbf{T}_{q|H_1}$. Substituting these estimates into (6) and (7), respectively, the ratio in (9) becomes

$$\Lambda_G(\mathbf{Z}) = \prod_{q=1}^{Q} \left[\frac{\|\mathbf{T}_{q|H_0}\|^{K_q+1}}{\|\mathbf{T}_{q|H_1}\|^{K_q+1}} \right]. \tag{10}$$

Next, we define a matrix using only the secondary data as

$$\mathbf{S}_q = \sum_{k=1}^{K_q} \mathbf{z}_q(k)\mathbf{z}_q^{\mathrm{H}}(k) \tag{11}$$

and using the same manipulations as in [7], we find that the signal estimates that maximize the ratio in (10) are $\hat{b}_q = \mathbf{s}_q^{\mathrm{H}}\mathbf{S}_q^{-1}\mathbf{z}_q / \mathbf{s}_q^{\mathrm{H}}\mathbf{S}_q^{-1}\mathbf{s}_q$. With these estimates, the multistatic GLRT is

$$\Lambda_G(\mathbf{Z}) = \prod_{q=1}^{Q} \left(\frac{1 + \mathbf{z}_q^{\mathrm{H}}\mathbf{S}_q^{-1}\mathbf{z}_q}{1 + \mathbf{z}_q^{\mathrm{H}}\mathbf{S}_q^{-1}\mathbf{z}_q - \dfrac{|\mathbf{s}_q^{\mathrm{H}}\mathbf{S}_q^{-1}\mathbf{z}_q|^2}{\mathbf{s}_q^{\mathrm{H}}\mathbf{S}_q^{-1}\mathbf{s}_q}} \right)^{K_q+1}$$

$$= \prod_{q=1}^{Q} (l_q)^{K_q+1}. \tag{12}$$

C. Multistatic Adaptive Matched Filter

The difference between the GLRT derivation and the procedure for deriving the adaptive matched filter (AMF) test statistic is the starting assumption for the interference covariance matrix. In the case of the multistatic GLRT, it is assumed that the noise statistics are unknown and must be estimated. In the case of the multistatic AMF, the noise statistics are assumed known, but then an estimate is substituted into the final form of the test statistic. This simplifies the derivation and provides a simpler test statistic.

As in the GLRT, the derivation begins with the LRT of (9). Since the $\mathbf{M}_q$s are treated as known quantities, however, terms in the LRT attributed to the secondary data cancel each other in the numerator and denominator. Thus, the LRT can be simplified to

$$\Lambda(\mathbf{Z}) = \Lambda(\mathbf{z}_1, \mathbf{z}_2, \ldots, \mathbf{z}_Q) = \prod_{q=1}^{Q} \frac{f_q(\mathbf{z}_q \mid H_1)}{f_q(\mathbf{z}_q \mid H_0)}. \tag{13}$$

Substituting in the Gaussian pdfs, simplifying, and taking the logarithm yields

$$\gamma = \ln(\Lambda) = \sum_{q=1}^{Q} (2\,\mathrm{Re}\{b_q^* \mathbf{s}_q^{\mathrm{H}}\mathbf{M}_q^{-1}\mathbf{z}_q\} - |b_q|^2 \mathbf{s}_q^{\mathrm{H}}\mathbf{M}_q^{-1}\mathbf{s}_q). \tag{14}$$

Again, we can maximize this expression with respect to the unknown signal amplitudes by maximizing each component of the summation. Therefore, we need to maximize

$$\gamma_q = 2\,\mathrm{Re}\{b_q^* \mathbf{s}_q^{\mathrm{H}}\mathbf{M}_q^{-1}\mathbf{z}_q\} - |b_q|^2 \mathbf{s}_q^{\mathrm{H}}\mathbf{M}_q^{-1}\mathbf{s}_q \tag{15}$$

with respect to b_q, which results in

$$\hat{b}_q = \frac{\mathbf{s}_q^{\mathrm{H}}\mathbf{M}_q^{-1}\mathbf{z}_q}{\mathbf{s}_q^{\mathrm{H}}\mathbf{M}_q^{-1}\mathbf{s}_q}. \tag{16}$$

The result of (16) represents the same maximum likelihood estimate for the target amplitude that we derived for the GLRT derivation except that here the covariance matrix is still assumed to be known. Substituting (16) into (14) for each observation platform yields

$$\gamma_{\mathrm{AMF}} = \sum_{q=1}^{Q} \frac{|\mathbf{s}_q^{\mathrm{H}}\mathbf{M}_q^{-1}\mathbf{z}_q|^2}{\mathbf{s}_q^{\mathrm{H}}\mathbf{M}_q^{-1}\mathbf{s}_q}. \tag{17}$$

Finally, the AMF approach of [8] calls for substituting in the maximum likelihood estimate of the interference covariance matrix computed from the secondary data. Thus, the multistatic AMF is

$$\gamma_{\mathrm{AMF}}(\mathbf{Z}) = \sum_{q=1}^{Q} \frac{|\mathbf{s}_q^{\mathrm{H}}\hat{\mathbf{M}}_q^{-1}\mathbf{z}_q|^2}{\mathbf{s}_q^{\mathrm{H}}\hat{\mathbf{M}}_q^{-1}\mathbf{s}_q} \tag{18}$$

where

$$\hat{\mathbf{M}}_q = \frac{1}{K_q} \sum_{k=1}^{K_q} \mathbf{z}_q(k)\mathbf{z}_q^{\mathrm{H}}(k). \tag{19}$$

D. Properties of the Test Statistics

In order to set the threshold using the Neyman-Pearson criterion, knowledge of the probability distribution of the test statistic under the null hypothesis is required. Taking the logarithm of (12), we have

$$\ln[\Lambda_G(\mathbf{Z})] = \sum_{q=1}^{Q} \ln[(l_q)^{K_q+1}] = \sum_{q=1}^{Q} (K_q + 1)\ln(l_q). \tag{20}$$

Each l_q term in (12) is equivalent to the monostatic GLRT of [7] where the probability of false alarm (P_{fa}) for a single data set is shown to be

$$P_{\mathrm{fa}} = \Pr\{l_q \geq l_0\} = \int_{l_0}^{\infty} f_q(l_q)dl_q = (l_0)^{N_q-1-K_q}. \tag{21}$$

Since $\Pr\{l_q > l_0\} = \Pr\{\ln(l_q) > \ln(l_0)\}$, we define $x_q = \ln(l_q)$ and $x_0 = \ln(l_0)$ and rewrite (21) as

$$P_{\mathrm{fa}} = \Pr\{x_q \geq x_0\} = \int_{x_0}^{\infty} f_q(x_q)dx_q = (\exp(x_0))^{N_q-1-K_q}. \tag{22}$$

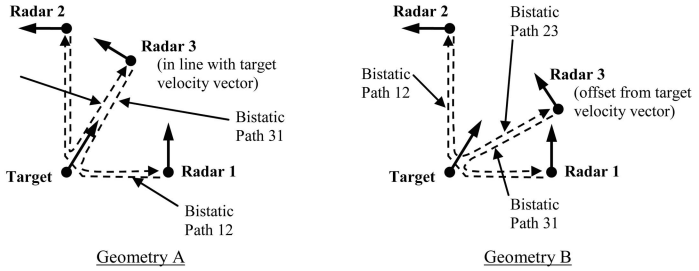

Fig. 1. Multistatic geometries used for simulation of three-platform systems.

Next, if $F_q(x_0)$ is the cumulative distribution function (CDF) of the random variable x_q, then $F_q(x_0) = 1 - P_{\text{fa}}$. Using the right hand side of (22) for P_{fa} and taking the derivative of the cumulative distribution function (CDF), the pdf of x_q under H_0 is

$$f_q(x_q) = (K_q + 1 - N_q)\exp(-x_q[K_q + 1 - N_q]). \tag{23}$$

Therefore,

$$x_q = \ln(l_q) \tag{24}$$

is exponentially distributed with $\mathrm{E}[x_q] = 1/(K_q + 1 - N_q)$, and $(K_q + 1)\ln(l_q)$ is exponentially distributed with a mean of $(K_q + 1)\mathrm{E}[x_q]$.

Based on the above, the logarithm of (12) results in a test statistic that is the sum of independent exponential random variables. Since K_q and N_q may be different for each platform, the mean of each term in the resulting statistic may be different. Hence, calculating the probability of false alarm for the multistatic GLRT requires the distribution for a weighted sum of exponential variates, which is presented in [9]–[11]. Furthermore, we can now use these relationships to determine the CFAR properties of the multistatic GLRT. The pdf of a weighted sum of independent exponential variates depends only on the weights (means) of the individual terms. Since the above expression for the mean of a single term does not depend on any clutter statistics, it follows that the complete multistatic GLRT is a CFAR test. The pdf of the test output under H_0 depends only on the snapshot length and number of secondary snapshots for each platform.

It is not unexpected that the multistatic GLRT is a CFAR test since the independence assumptions reduce the test to a summation of terms that individually are equivalent to the CFAR test of [7]. Similarly, the multistatic AMF consists of a summation in which the individual terms are themselves CFAR. Again, in [8] the individual terms are proven to be functions of K_q and N_q, but not functions of the underlying interference statistics. The summation of these individual test statistics into a single statistic preserves the CFAR property of the multistatic AMF. Unfortunately, a closed-form solution for the probability of false alarm for the single-platform AMF was not presented in [8]. In order to calculate the probability of false alarm for the single-platform case, Robey [12] performs a numerical integration over the pdf of a random loss factor ρ, which is beta distributed. With this being the case, a closed-form expression for the probability of false alarm of the multistatic AMF is currently unavailable, and in our results below we have set detection thresholds for this test empirically.

III. RESULTS

In this section, the performance characteristics of the two multistatic detection methods are evaluated and compared. Performance was evaluated numerically using a multistatic STAP Monte Carlo simulation. First, we evaluate probability of detection (P_{d}) as a function of input SNR for tests using one, two, and three radars in a multistatic system. Initially, the target has fixed amplitude as observed by all radars in the system. The geometry used for the first scenario is geometry A, shown in Fig. 1. As Fig. 1 indicates, each of the three radars observes the scene from a different aspect. Each radar's look direction is perpendicular to its velocity vector, and the hypothesized target is assumed to be in the center of the beam for each radar. After performing this experiment for the nonfluctuating target model, the same performance is reviewed for a fluctuating target model.

In the first set of tests, only monostatic data collections are employed. In other words, each radar platform transmits and receives its own waveform, but does not observe the reflections due to transmissions from the other platforms. The data from each platform are still used to produce a joint test statistic. In subsequent results, we consider the use of bistatic data to improve the DO of the system.

For this simulation, each radar platform has the same operating frequency, 450 MHz, and pulse repetition frequency (PRF), 600 Hz. (We assume that some type of signal coding enables each receiver to separate out reflections due to its own transmitter. In practice, the simplest way to do this might be to transmit on different bands.) All radars are traveling at 60 m/s in the direction indicated in geometry A of Fig. 1. Each radar platform uses a 5-element antenna array with half-wavelength spacing. The interference

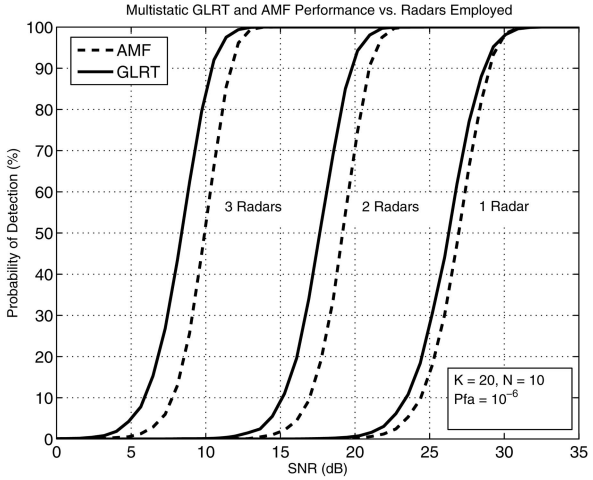

Fig. 2. Multistatic GLRT and AMF performance as function of Q.

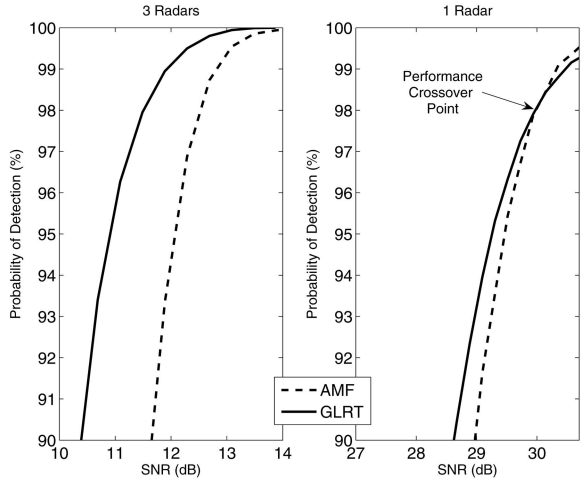

Fig. 3. GLRT versus AMF performance at high probability of detection.

covariance matrices $\mathbf{M}_q$ are calculated using arbitrary ground reflectivity profiles in such a way that each ground profile is unique for each radar perspective. Clutter-to-noise ratios (CNRs) ranged from 47 to 53 dB. No antenna alignment or ownship position errors were considered; therefore, target steering vectors were assumed to be accurate. A small amount of internal clutter motion (ICM) has been added to the interference covariance matrices to simulate surface wind conditions.

The first experiment looks at multistatic GLRT and AMF methods where all platforms have 10 deg of freedom and use 20 secondary data snapshots to form a sample covariance matrix. This particular setup is used so that results for a single platform will be comparable with those of [8]. The target has the same constant amplitude for all radar observation platforms. As can be seen in Fig. 2, the performance of the combined system improves as the number of radar platforms increases, regardless of the method employed. Also, the multistatic GLRT performs slightly better than the multistatic AMF, and the margin of that performance advantage increases as the number of platforms increases.

Fig. 3 expands the scale on the single-radar and three-radar cases of Fig. 2 to show the AMF/GLRT performance crossover phenomenon discussed in [8]. It is interesting to note that the performance crossover seems to be unique to the single-radar case. It is possible that the crossover point still exists for the multistatic system, but if so, it is located at a P_{d} that increases as the number of platforms is increased.

Since the multistatic system consists of multiple moving airborne platforms, a fading target model better represents the radar cross section (RCS) fluctuations associated with multifaceted complex target returns. Therefore, the next experiment uses the same parameters as those used in Fig. 2, but employs a Swerling I target fluctuation model to

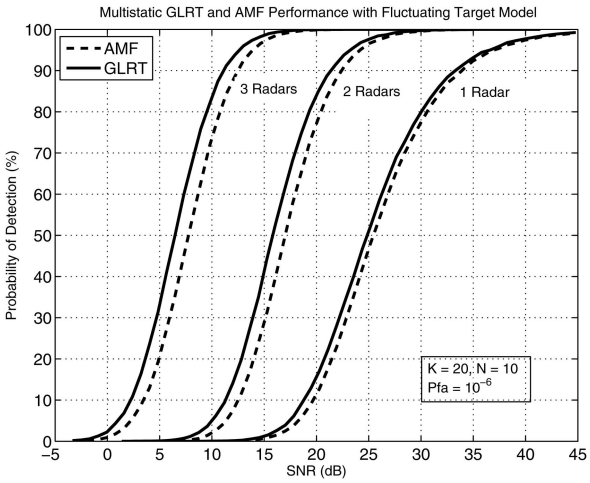

Fig. 4. GLRT and AMF performance for Swerling I target model.

simulate target fades with respect to target orientation. The target fades are modeled as being independent from radar to radar, which is a good assumption if the radar platforms are widely separated. However, we should point out that the detection statistics of Section II were derived under the assumption of deterministic but unknown target amplitudes, not the Swerling I model. Hence, we are applying a somewhat mismatched signal model, but this approach is not without precedent. The behavior of the monostatic GLRT and AMF under a Swerling I target model was evaluated in [8]. Moreover, one of the significant benefits of multistatic radar is the diversity gain associated with random target fluctuations, which implies a fluctuating target model.

The performance curves in Fig. 4 become steeper as more radar platforms are added to the system. This is due to the fact that multistatic observations of a fluctuating target enhance the likelihood that the target will be observed from an aspect where

its RCS is high. In a nonfluctuating target model, multistatic observation provides little benefit at low SNR because each platform observes low SNR. With a fluctuation model, however, the probability that the target is faded for all radar platforms is low. Also note in Fig. 4 that the performance advantage of the GLRT over the AMF again becomes larger as the number of platforms increases, just as it did in the nonfluctuating target model case.

An alternative way of looking at diversity gain comes from looking at the metrics used to characterize MIMO communication channels (or other systems using diversity reception). In communication theory, probability of outage is defined as the probability that SNR drops to a level at which communication becomes unreliable. The diversity order (DO) of a communication system is defined as the asymptotic (as SNR approaches infinity) slope of probability of outage versus SNR [13] plotted on a log-log scale:

$$\mathrm{DO} = -\lim_{\mathrm{SNR}\to\infty} \frac{\log(P_{\mathrm{outage}})}{\log(\mathrm{SNR})}. \tag{25}$$

In MIMO communication systems, this slope is equal to the number of independent channels employed by the system.

In comparison, probability of miss (P_{m}) is the probability that a radar system fails to detect a target that is present. This radar performance metric is directly analogous to probability of outage in communication systems. Therefore, the asymptotic log-log rate at which P_{m} decreases in a multistatic radar system should be equal to the number of independent target fluctuations observed by the system. The radar equivalent of DO is then

$$\mathrm{DO} = -\lim_{\mathrm{SNR}\to\infty} \frac{\log(P_m)}{\log(\mathrm{SNR})}. \tag{26}$$

Fig. 5 uses the same data that were used to create Fig. 4, but displays $\log(P_m)$ as a function of SNR to determine if this asymptotic relationship exists in a multistatic STAP system. As Fig. 5 indicates, DO is directly linked to the number of independent observations obtained by the multistatic system. As SNR becomes large, the performance curves in Fig. 5 become linear in the log-log scale. Moreover, for each 10 dB of SNR increase within the linear region of these curves, P_{m} decreases by Q factors of 10 where Q is the number of data sets containing independent target fluctuations.

In the previous simulations, all observations were collected using the monostatic scenario described above. That is, each platform only received reflections due to its own transmitted waveform. Next, we consider how detection can be improved by adding data collected from the available bistatic propagation paths. If two platforms observe the target from different aspects, it is reasonable that the bistatic

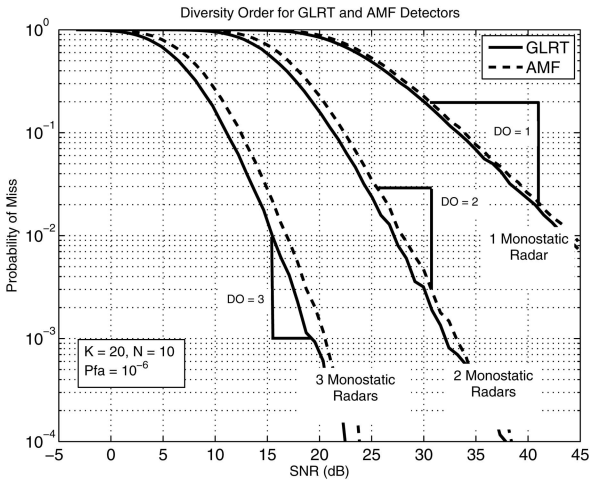

Fig. 5. Multistatic radar DO as function of number of platforms.

target fluctuation would be independent from the fluctuations observed over the two monostatic paths. Thus, the bistatic paths provide an opportunity to increase the number of independent target fluctuations observed by the system without increasing the number of radar platforms.

In the next simulation, the multistatic system exploits both monostatic data collection and bistatic data collection geometries. We only consider a single direction for each bistatic path since the target fluctuation in the reverse direction would not be independent if it is due to a transmitter operating on the same frequency band with different temporal coding. If there are N radar platforms, this assumption results in $Q = N(N+1)/2$ independent target fluctuations. Alternatively, if we were to assume that each transmitter operates on a different frequency band such that the frequency dependence of the target's reflection coefficient results in nonreciprocal target fluctuations, we could obtain $Q = N^2$ independent fluctuations. For the purposes of this study, any resolution issues associated with wide bistatic angles are ignored. Four geometries are considered in Fig. 6. We consider the three-platform scenarios of geometry A and geometry B where only monostatic paths are considered. We also consider a two-platform system consisting of radars 2 and 3 in both geometry A and B but allow for the bistatic path between the two. All four scenarios have three unique propagation paths; hence, all scenarios have a DO of three.

Despite constant DO, the four collection geometries have different performance levels that can be understood by considering the geometry of each. The shifts in the curves are a result of differences in geometry with respect to the target's velocity vector. Both configurations from geometry A outperform their corresponding configuration from geometry B because the third radar in geometry A is in better position to observe the target's Doppler shift.

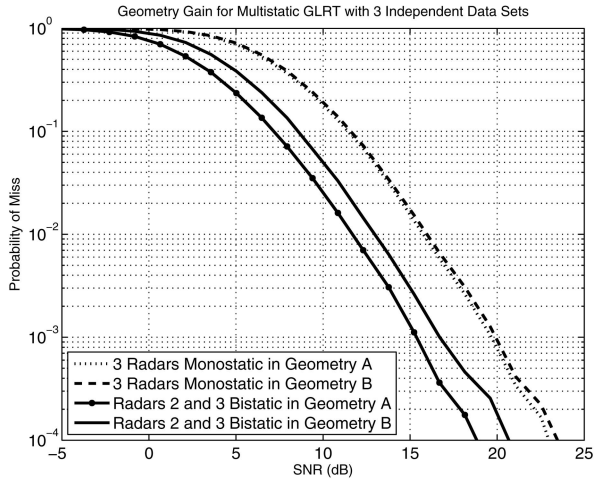

Fig. 6. Example of geometry gain for multistatic GLRT with DO of three but different physical configurations.

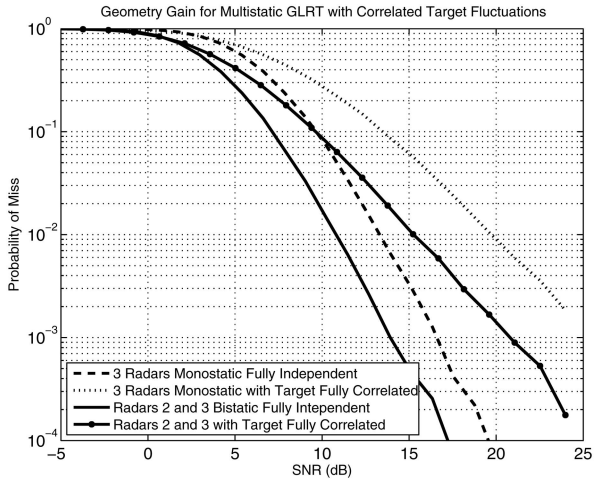

Fig. 7. DO comparison for correlated versus independent target fluctuations.

It is clear that when colored interference such as ground clutter is present, target-radar geometry plays a key role in determining the diversity benefit realized by the system. We can exploit the fact that the P_{m} curves are asymptotically linear to quantify this controlling factor, which we term geometry gain. If DO is the asymptotic slope of the P_{m} curves, we define geometry gain as the shift between curves in the asymptotic, linear-slope region. Thus, we can say, for example, that the two-platform system in geometry A has a geometry gain of nearly 5 dB over the three-platform system in geometry B, or that the three-platform geometry A configuration has a geometry gain of less than 1 dB over the three-platform geometry B configuration. These relative shifts in the performance curves reflect the fact that good geometries reach their asymptotic performance and realize their diversity benefit at lower SNR than poor geometries.

Finally, we consider the case where multiple radar platforms are available, but are located in a configuration where the target reflections are not always independent. This may occur, for example, when two of the radar platforms observe the target from nearly the same aspect angle. The angle span over which the target reflections are correlated depends on target properties as well as whether the same frequency band is being used by the two platforms. For now, we force two of the target reflection coefficients in the simulation to be equal. It is expected that perfect correlation between two data sets will reduce DO by one, which is exactly what is seen in Fig. 7. Defining a signal coefficient vector as $\mathbf{b} = [b_1 \;\; b_2 \cdots b_Q]^{\mathrm{T}}$, DO will, in general, be directly related to the rank of the signal coefficient covariance matrix, $\mathrm{E}[\mathbf{b}\mathbf{b}^{\mathrm{H}}]$.

IV. CONCLUSIONS

The analysis shows that the multistatic GLRT test statistic outperforms the AMF method, especially as the number of platforms collecting independent observations is increased. Furthermore, a closed-form expression for the probability of false alarm is available for the multistatic GLRT but not for the multistatic AMF.

We have used asymptotic P_{m} performance to isolate and quantify the differences between geometry gain and DO. We have noted that the number of independent observations collected by a multistatic system can be increased by incorporating bistatic configurations between radar platforms, thereby increasing the DO of the system without additional platforms. When only monostatic data collections are employed by the multistatic system, the number of independent looks increases linearly with the number of observing platforms. However, when each unique bistatic path is also included in the test statistic, the DO of the system increases roughly as the square of the number of platforms according to either $Q = N(N+1)/2$ or $Q = N^2$, depending on assumptions in the target fluctuation model.

DONALD P. BRUYÈRE
NATHAN A. GOODMAN
Dept. of Electrical and Computer Engineering
University of Arizona
1230 E. Speedway Blvd.
Tucson, AZ 85721
E-mail: (goodman@ece.arizona.edu)

REFERENCES

[1] Melvin, W. L.
A STAP overview.
IEEE AES Systems Magazine, **19**, 1, pt. 2 (Jan. 2004), 19–35.

[2] Ward, J.
Space-time adaptive processing for airborne radar.
MIT Lincoln Laboratory, Lexington, MA, Technical Report 1015, Dec. 1994.

[3] Brennan, L. E., and Reed, I. S.
Theory of adaptive radar.
IEEE Transactions on Aerospace and Electronics Systems, **AES-9**, 2 (Mar. 1973), 237–252.

[4] Goodman, N. A., and Bruyere, D.
Optimum and decentralized detection for multistatic airborne radar.
IEEE Transactions on Aerospace and Electronics Systems, **43**, 2 (Apr. 2007), 806–813.

[5] Fishler, E., et al.
Spatial diversity in radars-models and detection performance.
IEEE Transactions on Signal Processing, **54**, 3 (Mar. 2006), 823–838.

[6] Fishler, E.
MIMO Radar: An Idea Whose Time Has Come.
In *Proceedings of the IEEE Radar Conference*, Apr. 2004, 71–78.

[7] Kelly, E. J.
An adaptive detection algorithm.
IEEE Transactions on Aerospace and Electronics Systems, **AES-22**, 1 (Mar. 1986), 115–127.

[8] Robey, F. C., Fuhrmann, D. R., Kelly, E. J., and Nitzberg, R.
A CFAR adaptive matched filter detector.
IEEE Transactions on Aerospace and Electronics Systems, **28**, 1 (Jan. 1992), 208–216.

[9] Ali, M. M., and Obaidullah, M.
Distribution of linear combination of exponential variates.
Communications in Statistics—Theory and Methods, **11**, 13 (1982), 1453–1463.

[10] Hahn, G. J., and Shapiro, S. S.
Statistical Models in Engineering.
New York: Wiley, 1994.

[11] Johnson, N. L., Kotz, S., and Balakrishnan, N.
Continuous Univariate Distributions (2nd ed.).
New York: Wiley, 1994.

[12] Robey, F. C.
A covariance modeling approach to adaptive beamforming and detection.
MIT Lincoln Laboratory, Lexington, MA, Technical Report 918, July 1991.

[13] Varadarajan, B., and Barry, J. R.
The rate-diversity trade-off for linear space-time codes.
Proceedings 56th Vehicular Technology Conference, vol. 1, Sept. 2002, 67–71.

Pulse Compression for a Simple Pulse

A new pulse compression method for a simple pulse is proposed. The proposed method has a filter with impulse response $h(t)$ whose Fourier transform $H(f)$ is given by $D(f)/S(f)$, where $D(f)$ is the Fourier transform of desired output waveform $d(t)$ and $S(f)$ is the Fourier transform of input signal $s(t)$. Frequency characteristics $D(f)$ are considered not to make $H(f)$ divergent, since frequency characteristics $S(f)$ have zero points at the multiplication number of the reciprocal number of the input pulsewidth. The proposed method has an advantage because it can be compressed to the arbitrary pulsewidth given by waveform $d(t)$ and can be designed for compressed output with small peak sidelobe level.

I. INTRODUCTION

Pulse compression has been employed to simultaneously satisfy the requirements of maximum detection range and range resolution [1]. Generally, pulsewidth compressed by these methods approximately equals the reciprocal of the main spectrum width where the spectrum energy of the transmitting pulse is concentrated. Therefore, it is necessary to spread the bandwidth of the transmitted pulse to obtain narrower range resolution. It is important to obtain narrower range resolution without wider bandwidth of the transmitted pulse because this leads to the effective use of radio waves. Many investigators have studied pulse compression techniques [2]. R. H. Barker proposed codes with an autocorrelation function whose peak sidelobe level is only 1 [3]. J. Lindner [4] and M. N. Cohen et al. [5] investigated optimum binary codes that have an autocorrelation function with peak sidelobe levels which are the smallest possible level for a given code length in the relatively small compression ratio region (optimum binary codes). Rao and Reddy investigated the binary codes of relatively long code length that have an autocorrelation function with comparatively small peak sidelobe levels (PSLs) [6]. G. Coxson and J. Russo extended the upper limit of the length to 70 [7]. These methods are compressed to pulse wide given approximately by the reciprocal of the main spectrum of the transmitted pulse which is modulated. L. K. Cuomo tried to compress an input pulse into a narrower pulsewidth

Manuscript received October 2, 2006; revised May 10, 2007; released for publication July 17, 2008.

IEEE Log No. T-AES/44/4/930747.

Refereeing of this contribution was handled by V. C. Chen.